

Spinon Singlet: Microscopic Mechanism of d -Wave Pairing in a Partially-Filled Stripe

Jia-Long Wang,¹ Shi-Jie Hu,^{1,2,*} and Xue-Feng Zhang^{3,4,†}

¹Beijing Computational Science Research Center, Beijing 100193, People's Republic of China

²Department of Physics, Beijing Normal University, Beijing 100875, People's Republic of China

³Center of Quantum Materials and Devices, Chongqing University, Chongqing 401331, China

⁴Department of Physics and Chongqing Key Laboratory for Strongly Coupled Physics, Chongqing University, Chongqing 401331, China

Significant research advances have led to a consensus that the Fermi-Hubbard model and its extended variants are archetypal frameworks for elucidating the intertwined relationship between stripe orders and superconductivity in hole-doped high- T_c materials. Notably, the Hubbard quantum simulator has recently achieved several remarkable breakthroughs, e.g., being successfully cooled down to the cryogenic regime and enabling the observation of stable fluctuating stripes. However, the microscopic mechanism behind d -wave pairing of electrons in the presence of stripes at low temperatures remains poorly understood due to the intricate interplay among the strongly correlated effects and non-negligible thermal fluctuations. Here, we conduct a close investigation of a partially-filled stripe in the representative t - J and Fermi-Hubbard models with both numerical and analytical methods. Analogous to quantum gas microscopy, the perfect sampling technique allows us to obtain the high-confidence statistics of the Fock basis states appearing in the ground-state wavefunction. In a refreshing physical paradigm, these data demonstrate that two spinons with opposite chiralities tend to spontaneously pair into a singlet state, which naturally gives rise to the d -wave pairing pattern. Then, using the effective theory of quantum colored string, we reconstruct the wavefunction and determine the nature of spinon pairing and its connection to the d -wave pairing pattern. Furthermore, spinon singlet pairs enable the establishment of a long-range pair-pair correlation between double stripes. Our work offers new insights into the role of stripe orders in mediating d -wave superconductivity and paves the way for further exploration of multi-stripe-mediated pairing mechanisms in the Fermi-Hubbard model.

Introduction.—Establishing the correct microscopic mechanisms for the pairing process is a crucial step in understanding high- T_c superconductivity [1–6]. In hole-doped cuprates, experiments have provided strong support for the idea of local electron pairing within the widely observed d -wave superconducting states [7–9]. Numerical simulation results, which are consistent with experimental detections [10, 11], have also suggested an intertwined relationship between the stripe phase and superconductivity [12, 13], extending beyond the Hubbard model [14–18] to include a wide range of models, e.g., t - J , t - t' - J , etc. [19–26]. More recently, simulations of the Hubbard model using density matrix renormalization group (DMRG) and quantum Monte Carlo (QMC) methods have revealed the coexistence of d -wave superconductivity with partially-filled stripes [17]. It was also found that “Cooper pairs” are not uniformly distributed in space, but tend to accumulate at the hole-rich stripes [27], challenging Anderson’s resonating valence bond (RVB) paradigm [28]. Meanwhile, the origin of the pseudogap appears to be closely related to the melting of the stripe phase with pre-pairing [29, 30]. Therefore, it is believed that the single-band Hubbard model and its t - J extensions can capture the main physics of high- T_c superconductivity.

Unveiling the mysteries of the Fermi-Hubbard model is also one of the critical goals in quantum simulations. By constructing an optical lattice with counterpropagating lasers, the ultra-cold fermions can be trapped [31–35], and their interactions can be flexibly adjusted, allowing for the engineering of various Hubbard-like models [36]. As the temperature is

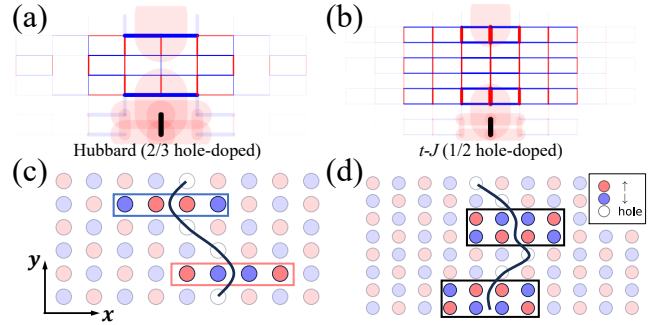


FIG. 1. The PPC function, starting from the target y -bond (black line with a width corresponding to a magnitude of 0.01), is calculated with DMRG method for (a) the Hubbard model including the NNN hopping $t' = -0.2$ with $U = 12$ and $\mathbf{L} = (L_x, L_y) = (9, 6)$. (b) the t - J model at $J = 0.6$ and $\mathbf{L} = (11, 8)$. The width of the red and blue ribbons at each bond represents the magnitude of the positive and negative PPC, respectively. The largest-weight snapshots are obtained by perfect sampling the ground-state wavefunction for (c) the Hubbard model and (d) the t - J model. The spinons with chirality \uparrow (\downarrow) are highlighted with red (blue) rectangles, and their pairing is marked with a black frame.

reduced close to the critical temperature of the superconducting phase [35], the potential of quantum simulations gradually emerges [37, 38]. Quantum gas microscopy [38], as a characteristic method, provides an ideal tool for instantaneously capturing the distribution of fermions [31, 33], so microscopic dynamics can be observed directly. Such in-situ detection is particularly vital for strongly correlated systems [39], where the quasi-particle size is often comparable to the lattice spacing, e.g., spinon, Majorana, or fracton. Recently, the formation of individual stripes has been directly observed in a quan-

* Corresponding author: shijiehu@csrc.ac.cn

† Corresponding author: zhangxf@cqu.edu.cn

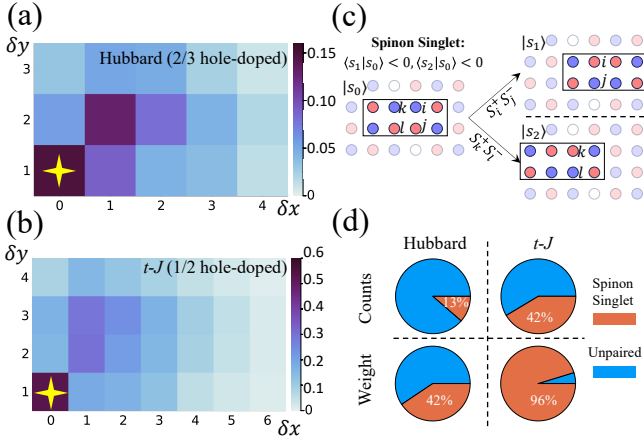


FIG. 2. (a,b) Spinon correlation function with spinon distances $(\delta x, \delta y)$ in the x and y directions. (c) Two spin-flipping processes for identifying the “spinon singlet”. (d) The statistics of counts and weights of snapshots for different categories. All the data are obtained via the perfect sampling technique, and the parameters are the same as those used in Fig. 1.

tum simulator [33]. However, the intricate interplay among electrons, multiple stripes, and thermal fluctuations creates a barrier to diagnosing the microscopic mechanism behind the d -wave pairing deep within the system.

In this manuscript, a partially-filled stripe on a cylinder of a square lattice is systematically analyzed using both numerical and analytic methods. As demonstrated in Figs. 1(a-b), simulated by the large-scale DMRG method, the pair-pair correlation (PPC) function $G_{b,b'} = \langle \Delta_b^\dagger \Delta_{b'} \rangle$ at bonds b and b' clearly shows the d -wave patterns around the stripe in both the Hubbard and t - J models. Specifically, $G_{b,b'}$ for a target y -bond and a distant x -bond exhibits a negative sign, as indicated by the blue ribbons. Then, with the help of the perfect sampling technique [40] and the effective theory of quantum color string (QCS) model (QCSM) [41], we find that the spinons (topological point-defects) prefer to pair in a singlet form along the QCS (topological line-defect) as shown in Fig. 1(c,d). These spinon singlets, which cooperate with quantum fluctuations along the fluctuating stripe, directly constitute the d -wave pairing pattern of electrons. Lastly, we exhibit the establishment of a long-range PPC function between two stripes.

Models.—The t - J model is described by the following Hamiltonian:

$$H = -t \sum_{\langle \ell, \ell' \rangle, \sigma} (f_{\ell, \sigma}^\dagger f_{\ell', \sigma} + \text{h.c.}) + J \sum_{\langle \ell, \ell' \rangle} \left(\mathbf{S}_\ell \cdot \mathbf{S}_{\ell'} - \frac{n_\ell n_{\ell'}}{4} \right), \quad (1)$$

where $f_{\ell, \sigma}^\dagger$, $f_{\ell, \sigma}$ and $n_{\ell, \sigma} = f_{\ell, \sigma}^\dagger f_{\ell, \sigma}$ represent the creation, annihilation, and particle number operators for an electron with spin $\sigma = \uparrow, \downarrow$ at site- ℓ , respectively. The term $\Delta_b = (f_{j, \downarrow} f_{i, \uparrow} - f_{j, \uparrow} f_{i, \downarrow})$ describes the annihilation of a singlet pair at bond $b = (i, j)$, where site i has a higher index than site j , according to the early site-labeling convention [41]. The particle number operator at site- ℓ is defined as $n_\ell = n_{\ell, \uparrow} + n_{\ell, \downarrow}$ with

double occupation forbidden, while the spin components at site- ℓ are given by $\mathbf{S}_\ell = (S_\ell^x, S_\ell^y, S_\ell^z)$. The nearest-neighboring (NN) hopping amplitude $t=1$ defines the energy unit. We set the spin interaction strength to $J=0.6$, which favors a π -phase stripe in the ground state. For the Hubbard model [17], we set the on-site repulsion strength to $U = 12$ and introduce a next-nearest-neighboring (NNN) hopping amplitude of $t' = -0.2$ to stabilize the partially-filled stripes.

Spinon Pairing.—In the quantum gas microscopy, the instant configuration of the fermions can be photoed using the fluorescence excited states [31]. Then, the tremendous snapshots can not only be used for quantum state tomography but also provide a visual physical picture for exploring the possible mechanism. A perfect sampling method can mimic such in-situ measurement and produce snapshots by randomly projecting the matrix product state (MPS) to different Fock states $|s\rangle$. Beyond quantum gas microscopy, the coefficient $\alpha_s = \langle s | \psi_D \rangle$ and the weight $|\alpha_s|^2$ can be extracted. In this work, five million snapshots are sampled at each parameter, which has been verified to be sufficient to draw robust conclusions [see details in the *End Matter*].

In Figs. 1(c,d), the largest-weight snapshot of both the Hubbard and t - J models serves rich information. A clear π -phase shift can be observed between two antiferromagnetic (AF) domains. The domain wall is constructed with two types of color particles (CPs): spinons $\uparrow\downarrow\uparrow$ or $\downarrow\uparrow\downarrow$ and holons $\uparrow \circ \downarrow$ or $\downarrow \circ \uparrow$. Including additional CP dual-holes $\uparrow \circ \circ \uparrow$ or $\downarrow \circ \circ \downarrow$ (discuss later), we can label them with color indices $c = \mathbf{r}, \mathbf{g},$ and \mathbf{b} . CPs can be further distinguished by their chiralities χ , defined according to the orientation of the leftmost spin. For example, for spinons, we have $\mathbf{r}_\uparrow = \uparrow\downarrow\uparrow$ and $\mathbf{r}_\downarrow = \downarrow\uparrow\downarrow$. Then, we can immediately find that the domain wall is a topological line-defect, which is also named as QCS composed of CPs [41]. In Fig. 1(d), four spinons spontaneously form two pairs with opposite chiralities reminiscent of singlet pairing.

In Figs. 2(a,b), the snapshot statistics of spinon distances show that two spinons most commonly appear at a distance $(\delta x, \delta y) = (0, 1)$ in both the Hubbard and t - J models, which directly supports the formation of spinon pairs discovered in Fig. 1(d). Interestingly, as depicted in Fig. 2(c), the spin exchange operation on a y -bond can move the spinon pair along the x -axis while simultaneously reversing their chirality sequence. Consequently, for a sample with a spinon pair $|s_0\rangle$, two states $|s_1\rangle$ and $|s_2\rangle$ can be generated by exchanging adjacent spins. We find that for almost all spinon pairs, both overlaps $\langle s_1 | s_0 \rangle$ and $\langle s_2 | s_0 \rangle$ are negative, marking the spinon pair as a “spinon singlet”. Sometimes, the singlet pair is destroyed due to the hole hopping and spin flipping [see *Supplementary Material (SM)*], and samples without a spin pair are grouped as “unpaired”, as shown in Fig. 1(c). The global snapshot statistics, shown in Fig. 2(d), reveal that nearly all spinon pairs form the singlets, as indicated by the negligible “invalid” ones. Meanwhile, although the count of “spinon singlet” is lower than that of the “unpaired” part, the ratio for “spinon singlet” in the weight statistics increases significantly.

Based on the perfect sampling data, we conclude that CPs tend to spontaneously organize into a stripe with a π -phase shift (i.e., a fluctuating QCS) in both the hole-doped t - J and

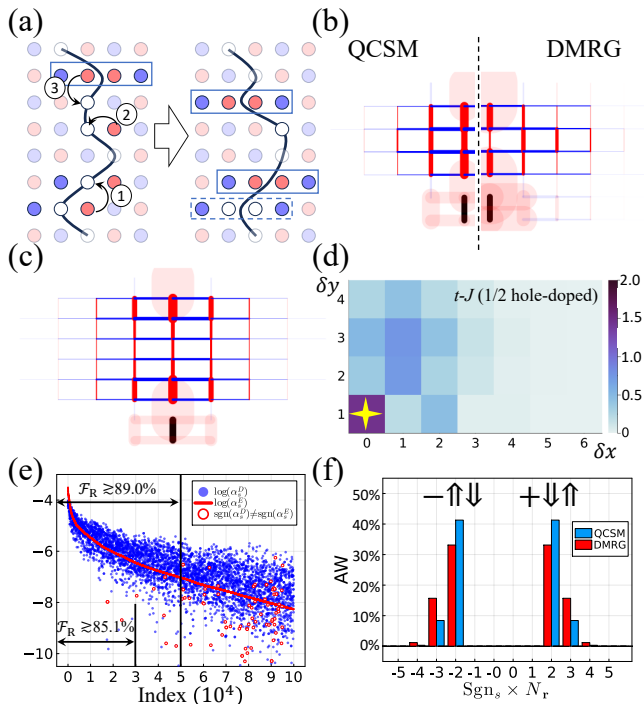


FIG. 3. (a) A schematic diagram shows the dynamics of QCS. The black arrows with numbers in circles label different dynamic processes. The dashed rectangle marks the dual-hole. (b) The PPC function $G_{b,b'}$ for a $2/3$ hole-doped stripe with $\mathbf{L} = (11, 6)$. (c) The PPC function $G_{b,b'}$ and (d) the spinon correlation function with different distances for a $1/2$ hole-doped stripe with $\mathbf{L} = (11, 8)$, calculated using the effective theory. (e) The amplitudes of expansion coefficients α_s^E and α_s^D , and (f) distributions of accumulated weights (AW) in $|\psi_E\rangle$ and $|\psi_D^\Omega\rangle$ with $\mathbf{L} = (11, 6)$.

Hubbard models. The spinons prefer to pair in a singlet form. Although quantum fluctuations can temporarily break the spinon singlet and ruin the local AF bonds, it can benefit the kinetic energy of spinon singlet via high-order processes. Later, we employ the effective theory of QCS [41] to uncover the connection between spinon singlets and d -wave pairing of electrons in the simplest case of the t - J model.

Theory of QCS.—As demonstrated in Fig. 3(a), the hopping process ① between two holons can create a spinon and a dual-hole, forming a \mathbf{r} - \mathbf{b} pair at adjacent rows. The QCS theory imposes a constraint that $\sum_c n_c = 1$ in each row. Within this restricted Hilbert space Ω , the stripe is described by a QCS. To account for the displacement of CPs along the x -axis between adjacent rows, an effective spin field $\Gamma^z \in \mathbb{Z}$ has to be included. Then, the effective model for a single QCS can be explicitly derived [see details in Ref. [41] and *End Matter*].

The AF background imposes an attractive diagonal interaction $\propto |\Gamma^z|$ between CPs, which plays as the tension energy of QCS. Besides the creation of a \mathbf{r} - \mathbf{b} pair and its reverse process, the electron hopping can deform the QCS and move the CPs, corresponding to processes ② and ③ in Fig. 3(a), respectively. The portion of spin exchange interaction relevant to the spinons has been considered in the effective model for a QCS. The remaining part, which only disrupts the local order in AF

domains, is argued to normalize the parameters of the effective model without affecting the main conclusions. In this work, only spin exchange interaction is adjusted to account for this renormalization effect [see *End Matter*].

Clearly, the potential energy suppresses the vibration of the QCS, while the quantum fluctuations introduced by the off-diagonal terms enhance this vibration. The interplay between the dynamics of CPs and local quantum fluctuations provides fruitful physics of the stripe. The ground-state wavefunction $|\psi_E\rangle = \sum_{s \in \Omega} \alpha_s^E |s\rangle$ of the effective QCS model is obtained through exact diagonalization (ED) with truncation $|\Gamma^z| \leq \Gamma_{\max}^z$, where α_s^E gives the expansion coefficient of the basis $|s\rangle$. Then, the PPC function shown in Fig. 3(b) with $\Gamma_{\max}^z = 9$ can be obtained, and QCS theory and DMRG results present a clear and consistent d -wave pattern. Meanwhile, the PPC function and spinon correlation of a $1/2$ hole-doped stripe are also calculated via the effective QCS model, and plotted in Figs. 3(c,d). They present similar distributions as the DMRG results in Fig. 1(b) and Fig. 2(b), respectively. These results demonstrate that the effective theory of QCS can semi-quantitatively describe the physics of a partially-filled stripe in the t - J model. Subsequently, it is anticipated that the relationship between d -wave pairing and spinon singlets is concealed within the wavefunction.

The QCS theory provides a competitive edge in analyzing the ground-state wavefunction and guides us in identifying the important Fock basis vectors contained within the space Ω . For $L_y = 6$ and $\Gamma_{\max}^z = 5$ in the effective theory, the Hilbert space dimension reaches 286,098, which is about 0.25% of the dimension used in the DMRG calculations $M = 16,384$. After projecting the wavefunction $|\psi_D\rangle$ onto Ω , we obtain the wavefunction $|\psi_D^\Omega\rangle = \sum_{s \in \Omega} \alpha_s^D |s\rangle$, where $\alpha_s^D = \langle s | \psi_D \rangle$. We then calculate the renormalized fidelity $\mathcal{F}_R = |\langle \psi_E | \psi_D^\Omega \rangle| / \sqrt{W}$, with $W = \langle \psi_D^\Omega | \psi_D^\Omega \rangle$. Using $M = 16,384$ in DMRG, we find $\mathcal{F}_R \approx 91.6\%$. As shown in Fig. 3(e) arranged in descending order of the amplitude $|\alpha_s^E|$, first 50,000 bases can provide very high fidelity, and meanwhile the signs of α_s^E and α_s^D are different in few, impressively.

The basis $|s\rangle$ can be characterized by the number of spinons N_r and the sign $\text{Sgn}_s \equiv \text{sgn}(\alpha_s^E)$. As shown in Fig. 3(f), the two-spinon bases with $N_r=2$ dominate the ground-state wavefunction, with the accumulated weights (AW) being symmetric with respect to $\text{Sgn}_s = \pm 1$. The distribution of three-spinon bases exhibits similar features, though with much lower weights, allowing us to neglect the contributions from other bases with $N_r > 3$. Given that the lower and upper spinons in the two-spinon bases carry chiralities χ_1 and χ_2 , we only need to consider configurations where $\chi_1 \neq \chi_2$, as the ground state lacks net magnetization. Interestingly, we find that Sgn_s for a two-spinon basis depends on the order of the chiralities, as highlighted in Fig. 3(f) (only $\approx 4\%$ unmatched). Specifically, $\text{Sgn}_s = \mp 1$ for $\chi_1 \chi_2 = \uparrow \downarrow$ and $\downarrow \uparrow$, respectively, which exactly match the sign structure of the spinon singlet. The three-spinon bases $|s\rangle$ arise from local vacuum fluctuations of the two-spinon bases $|s'\rangle$. If the emergent dual-hole is far from the two spinons in $|s\rangle$, the sign of its expansion coefficient is simply given by $\text{Sgn}_s = \text{Sgn}_{s'} \text{Sgn}_0$. Here, the sign Sgn_0 depends on the specifics of electron hopping in the

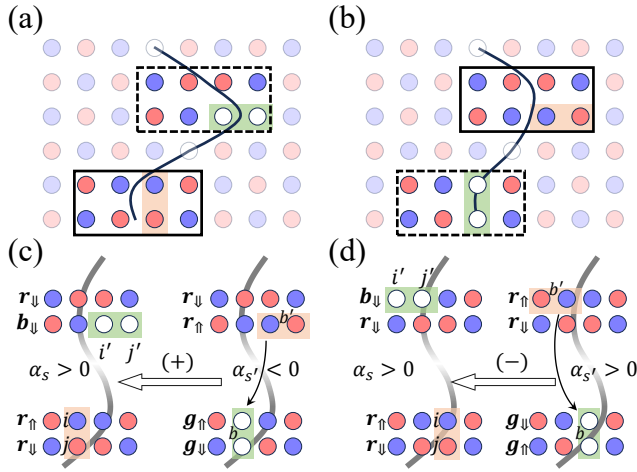


FIG. 4. Schematic diagrams illustrate a pair of (a) three-spinon and (b) two-spinon bases, which most significantly contribute to $G_{b,b'}$ for an x -bond b' and a y -bond b in a $2/3$ hole-doped stripe with $\mathbf{L} = (11, 6)$. The dashed rectangles enclose a dule-hole-spinon in (a) and a hole-hole pair in (b), respectively. The processes of moving an electron pair from x -bond b' to y -bond b (c) with and (d) without changing the chirality sequence are shown. The sign of $\text{Sgn}_\Delta = \pm$ is indicated above the black hollow arrows, corresponding to cases (c) without and (d) with spin exchange, respectively. The red (green) rectangle highlights the electron (hole) pair.

process from $\mathbf{g-g}$ to $\mathbf{r-b}$ [41]. Considering that the wavefunction $|\psi_E\rangle$ exhibits a robust sign structure of spinon singlets, a long-range d -wave pattern and a high fidelity with $|\psi_D\rangle$, we expect that the link between spinon singlets and d -wave pairing can be effectively diagnosed through a detailed analysis of wavefunction.

d -wave pairing.—At leading order, the PPC function receives a contribution $G_{b,b'}^{s,s'} = \alpha_s^* \alpha_{s'} \langle s | \Delta_b^\dagger \Delta_{b'} | s' \rangle$ from the basis $|s\rangle$ and $|s'\rangle$. At long distances, the sign of $G_{b,b'}^{s,s'}$ is given by $\text{Sgn}(G_{b,b'}^{s,s'}) = \text{Sgn}_s \text{Sgn}_{s'} \text{Sgn}_\Delta$, where the sign Sgn_Δ accounts for the spin exchange between Δ_b and $\Delta_{b'}$. Then, the PPC function between two y -bonds can be straightforwardly understood. The operator $\Delta_{b'}$ can annihilates two electrons with opposite spins at y -bond b' in a two-spinon basis $|s'\rangle$, and then Δ_b^\dagger fills two holes at y -bond b to generate the basis $|s\rangle$. If the chirality sequence $\chi_1 \chi_2$ in $|s\rangle$ and $|s'\rangle$ remains unchanged, then $G_{b,b'}^{s,s'} > 0$. However, if the chirality sequence is altered, the sign $\text{Sgn}_\Delta = -1$ must be included, compensating for the sign change caused by the altered chirality sequence. As a result, $G_{b,b'} > 0$ always for two y -bonds at long distances, owing to the spinon singlet state. Similarly, $G_{b,b'}$ is positive for two x -bonds, which is related to a spinon at x -bond b' and a dual-hole at another x -bond b (see *SM* for details).

✓ Most critical feature of d -wave pattern is negative PCC function $G_{b,b'}$ between a y -bond b and an x -bond b' . According to the effective theory, the nonzero contribution $G_{b,b'}^{s,s'}$ stems from a three-spinon basis $|s\rangle$ and a two-spinon basis $|s'\rangle$ at leading order. The number of these basis pairs $\{|s'\rangle, |s\rangle\}$ that contribute nonzero $G_{b,b'}^{s,s'}$ is quite limited, especially for bonds

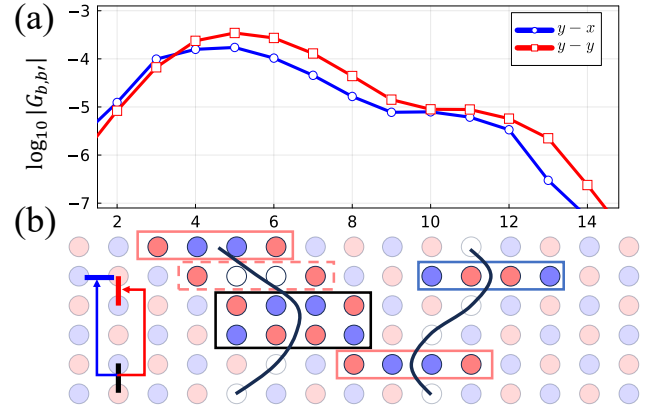


FIG. 5. (a) The PPC function $G_{b,b'}$ and (b) the largest-weight snapshot in the t - J model with $N_h = 8$ (two $2/3$ hole-doped stripes), and $\mathbf{L} = (15, 6)$, calculated using the DMRG method. The y - y (y - x) PPC function plotted in (a) corresponds to the correlation between the black target bond and the red y (blue x) bonds in the same row.

at long distances. This allows us to systematically identify all the contributing pairs and uncover the underlying microscopic pairing mechanism.

As demonstrated in Fig. 4(a), in the three-spinon basis $|s\rangle$ of the largest-weight basis pair, the spinon pair provides two electrons in the y -bond b and the $\mathbf{r-b}$ pair provides two holes in the x -bond b' . Then, after implementing $G_{b,b'}^{s,s'}$, they change into two holons and a spinon pair with different chirality sequence on the two-spinon basis $|s'\rangle$ shown in Fig. 4(b). Therefore, as analyzed in Fig. 4(c), if the chirality sequence of the spinon pair is different between $|s'\rangle$ and $|s\rangle$, the Sgn_Δ has to be $+1$. By analogy, the same chirality sequence requires $\text{Sgn}_\Delta = -1$ (see Fig. 4(d)). This analysis is also available for $G_{b,b'} < 0$ between an x -bond b and a y -bond b' at long distances (see more details in *SM*).

Conclusion and Outlook.—In both the Hubbard and t - J models, we identify a clear microscopic mechanism in which the spinon singlet, arising from a fluctuating two-spinon quantum colored string, leads to the emergence of d -wave pairing. Building on the quantum colored string scenario originally proposed by us [41], we have developed a bottom-up effective theory to describe the correlations between distant spinon pairs in the ground states of a partially-filled stripe.

We also extend the DMRG simulation to a wider system with two stripes. In Fig. 5(a), the PCC function, starting from the target y -bond near the left edge column, is enhanced by the left QCS and boosted by the right QCS over a long distance. From the largest-weight snapshot displayed in Fig. 5(b), we can clearly identify two QCSs and a complex interplay between the CPs. It appears to depict microscopic harmonic dance of spinons: a spinon singlet, activated within a QCS, tunneling into a neighboring QCS. Therefore, we are confident in conjecturing that the spinon pair may also serve as the elementary quasi-particle of the d -wave superconductivity in the Fermi-Hubbard model, with the QCS acting as the crucial “glue”. Definitely, the detailed microscopic mechanism in multiple stripes requires more future exploration.

Finally, we want to discuss the possible relation to the quantum simulations. Because of the rapid development of the quantum simulation based on the ultra-cold atoms [32, 37, 38], the local pairing of the spinons is expected to be clearly observed in the optical lattice via the quantum gas microscopy [38]. In addition, the distribution of the PPC function can also be checked in the mixD system that simulates the extended t - J model [42–44].

ACKNOWLEDGMENT

We would like to thank Tao Li, Hao Ding, and Yuan-Yao He for many helpful discussions, and the ad hoc editor of PRX in our previous paper[41] for the suggestion of the perfect sampling method. S. J. H. acknowledges funding from MOST Grant No. 2022YFA1402700, NSFC No. U2230402, NSFC Grant No. 12174020. X.-F. Z. acknowledges funding from the National Science Foundation of China under Grants No. 12274046, No. 11874094, No. 12147102, and No. 12347101, the Chongqing Natural Science Foundation under Grant No. CSTB2022NSCQ-JQX0018, the Fundamental Research Funds for the Central Universities Grant No. 2021CDJZYJH-003, and the Xiaomi Foundation/Xiaomi Young Talents Program.

-
- [1] J. Bardeen, L. N. Cooper, and J. R. Schrieffer, “Theory of superconductivity,” *Phys. Rev.* **108**, 1175–1204 (1957).
- [2] Elbio Dagotto, “Correlated electrons in high-temperature superconductors,” *Rev. Mod. Phys.* **66**, 763 (1994).
- [3] M. A. Kastner, R. J. Birgeneau, G. Shirane, and Y. Endoh, “Magnetic, transport, and optical properties of monolayer copper oxides,” *Reviews of Modern Physics* **70**, 897–928 (1998).
- [4] Patrick A. Lee, Naoto Nagaosa, and Xiao-Gang Wen, “Doping a mott insulator: Physics of high-temperature superconductivity,” *Rev. Mod. Phys.* **78**, 17 (2006).
- [5] B. Keimer, S. A. Kivelson, M. R. Norman, S. Uchida, and J. Zaanen, “From quantum matter to high-temperature superconductivity in copper oxides,” *Nature (London)* **518**, 179–186 (2015).
- [6] Qijin Chen, Zhiqiang Wang, Rufus Boyack, Shuolong Yang, and K. Levin, “When superconductivity crosses over: From bcs to bec,” *Rev. Mod. Phys.* **96**, 025002 (2024).
- [7] M. H. Hamidian, S. D. Edkins, Sang Hyun Joo, A. Kostin, H. Eisaki, S. Uchida, M. J. Lawler, E. A. Kim, A. P. MacKenzie, K. Fujita, Jinho Lee, and J. C. Séamus Davis, “Detection of a Cooper-pair density wave in $\text{Bi}_2\text{Sr}_2\text{CaCu}_2\text{O}_{8+x}$,” *Nature (London)* **532**, 343–347 (2016), arXiv:1511.08124 [cond-mat.supr-con].
- [8] Ivan Božović and Jeremy Levy, “Pre-formed Cooper pairs in copper oxides and LaAlO_3 — SrTiO_3 heterostructures,” *Nature Physics* **16**, 712–717 (2020).
- [9] Shusen Ye, Changwei Zou, Hongtao Yan, Yu Ji, Miao Xu, Zehao Dong, Yiwen Chen, Xingjiang Zhou, and Yayu Wang, “The emergence of global phase coherence from local pairing in underdoped cuprates,” *Nature Physics* **19**, 1301–1307 (2023), arXiv:2306.05926 [cond-mat.supr-con].
- [10] H. A. Mook, Pengcheng Dai, F. Dogan, and R. D. Hunt, “One-dimensional nature of the magnetic fluctuations in $\text{YBa}_2\text{Cu}_3\text{O}_{6.6}$,” *Nature (London)* **404**, 729–731 (2000), arXiv:cond-mat/0004362 [cond-mat.supr-con].
- [11] Zengyi Du, Hui Li, Sang Hyun Joo, Elizabeth P. Donoway, Jinho Lee, J. C. Séamus Davis, Genda Gu, Peter D. Johnson, and Kazuhiro Fujita, “Imaging the energy gap modulations of the cuprate pair-density-wave state,” *Nature (London)* **580**, 65–70 (2020), arXiv:2109.14033 [cond-mat.supr-con].
- [12] Eduardo Fradkin, Steven A. Kivelson, and John M. Tranquada, “Colloquium: Theory of intertwined orders in high temperature superconductors,” *Rev. Mod. Phys.* **87**, 457–482 (2015).
- [13] John M. Tranquada, “Spins, stripes, and superconductivity in hole-doped cuprates,” in *AIP Conference Proceedings* (AIP, 2013).
- [14] B. Zheng, Chia-Min Chung, Philippe Corboz, Georg Ehlers, Mingpu Qin, Reinhard M. Noack, Hao Shi, Steven R. White, Shiwei Zhang, and Garnet Kin-Lic Chan, “Stripe order in the underdoped region of the two-dimensional hubbard model,” *Science* **358**, 1155 – 1160 (2016).
- [15] Qiaoyi Li, Yuan Gao, Yuan-Yao He, Yang Qi, Bin-Bin Chen, and Wei Li, “Tangent space approach for thermal tensor network simulations of the 2d hubbard model,” *Phys. Rev. Lett.* **130**, 226502 (2023).
- [16] Alexander Wietek, Yuan-Yao He, Steven R. White, Antoine Georges, and E. Miles Stoudenmire, “Stripes, antiferromagnetism, and the pseudogap in the doped hubbard model at finite temperature,” *Phys. Rev. X* **11**, 031007 (2021).
- [17] Hao Xu, Chia-Min Chung, Mingpu Qin, Ulrich Schollwöck, Steven R. White, and Shiwei Zhang, “Coexistence of superconductivity with partially filled stripes in the Hubbard model,” *Science* **384**, eadh7691 (2024), arXiv:2303.08376 [cond-mat.supr-con].
- [18] Bo Xiao, Yuan-Yao He, Antoine Georges, and Shiwei Zhang, “Temperature Dependence of Spin and Charge Orders in the Doped Two-Dimensional Hubbard Model,” *Physical Review X* **13**, 011007 (2023), arXiv:2202.11741 [cond-mat.str-el].
- [19] Steven R. White and D. J. Scalapino, “Energetics of domain walls in the 2d t - j model,” *Phys. Rev. Lett.* **81**, 3227–3230 (1998).
- [20] Shoushu Gong, W. Zhu, and D. N. Sheng, “Robust d -wave superconductivity in the square-lattice t - j model,” *Physical Review Letters* **127**, 097003 (2021).
- [21] Chia-Min Chung, Mingpu Qin, Shiwei Zhang, Ulrich Schollwöck, and Steven R. White (The Simons Collaboration on the Many-Electron Problem), “Plaquette versus ordinary d -wave pairing in the t' -hubbard model on a width-4 cylinder,” *Phys. Rev. B* **102**, 041106 (2020).
- [22] Xin Lu, Feng Chen, W. Zhu, D. N. Sheng, and Shou-Shu Gong, “Emergent superconductivity and competing charge orders in hole-doped square-lattice t - j model,” *Phys. Rev. Lett.* **132**, 066002 (2024).
- [23] Yi-Fan Jiang, Thomas P. Devereaux, and Hong-Chen Jiang, “Ground-state phase diagram and superconductivity of the doped hubbard model on six-leg square cylinders,” *Phys. Rev.*

- B **109**, 085121 (2024).
- [24] Hong-Chen Jiang and Thomas P. Devereaux, “Superconductivity in the doped hubbard model and its interplay with next-nearest hopping t' ,” *Science* **365**, 1424–1428 (2019).
- [25] Yi-Fan Jiang, Jan Zaanen, Thomas P. Devereaux, and Hong-Chen Jiang, “Ground state phase diagram of the doped hubbard model on the four-leg cylinder,” *Phys. Rev. Res.* **2**, 033073 (2020).
- [26] Dai-Wei Qu, Bin-Bin Chen, Xin Lu, Qiaoyi Li, Shou-Shu Gong, Yang Qi, Wei Li, and Gang Su, “ d -wave superconductivity, pseudogap, and the phase diagram of t - t' - j model at finite temperature,” (2023), arXiv:2211.06322 [cond-mat.str-el].
- [27] Alexander Wietek, “Fragmented cooper pair condensation in striped superconductors,” *Physical Review Letters* **129**, 177001 (2022).
- [28] P. W. Anderson, “The resonating valence bond state in La₂CuO₄ and superconductivity,” *Science* **235**, 1196–1198 (1987).
- [29] Koen M. Bastiaans, Damianos Chatzopoulos, Jian-Feng Ge, Doohee Cho, Willem O. Tromp, Jan M. van Ruitenbeek, Mark H. Fischer, Pieter J. de Visser, David J. Thoen, Eduard F. C. Driessen, Teunis M. Klapwijk, and Milan P. Allan, “Direct evidence for Cooper pairing without a spectral gap in a disordered superconductor above T_c ,” *Science* **374**, 608–611 (2021), arXiv:2101.08535 [cond-mat.supr-con].
- [30] Fedor Šimkovic, Riccardo Rossi, Antoine Georges, and Michel Ferrero, “Origin and fate of the pseudogap in the doped Hubbard model,” *Science* **385**, eade9194 (2024), arXiv:2209.09237 [cond-mat.str-el].
- [31] Christie S. Chiu, Geoffrey Ji, Annabelle Bohrdt, Muqing Xu, Michael Knap, Eugene Demler, Fabian Grusdt, Markus Greiner, and Daniel Greif, “String patterns in the doped Hubbard model,” *Science* **365**, 251–256 (2019), arXiv:1810.03584 [cond-mat.quant-gas].
- [32] Muqing Xu, Lev Haldar Kendrick, Anant Kale, Youqi Gang, Geoffrey Ji, Richard T. Scalettar, Martin Lebrat, and Markus Greiner, “Frustration- and doping-induced magnetism in a Fermi-Hubbard simulator,” *Nature (London)* **620**, 971–976 (2023), arXiv:2212.13983 [cond-mat.quant-gas].
- [33] Dominik Bourgund, Thomas Chalopin, Petar Bojović, Henning Schlömer, Si Wang, Titus Franz, Sarah Hirthe, Annabelle Bohrdt, Fabian Grusdt, Immanuel Bloch, and Timon A. Hilker, “Formation of individual stripes in a mixed-dimensional cold-atom fermi-hubbard system,” *Nature* **637**, 57–62 (2025).
- [34] Hou-Ji Shao, Yu-Xuan Wang, De-Zhi Zhu, Yan-Song Zhu, Hao-Nan Sun, Si-Yuan Chen, Chi Zhang, Zhi-Jie Fan, Youjin Deng, Xing-Can Yao, Yu-Ao Chen, and Jian-Wei Pan, “Antiferromagnetic phase transition in a 3d fermionic hubbard model,” *Nature* **632**, 267–272 (2024).
- [35] Muqing Xu, Lev Haldar Kendrick, Anant Kale, Youqi Gang, Chunhan Feng, Shiwei Zhang, Aaron W. Young, Martin Lebrat, and Markus Greiner, “A neutral-atom hubbard quantum simulator in the cryogenic regime,” *Nature* (2025), 10.1038/s41586-025-09112-w.
- [36] Annette N. Carroll, Henrik Hirzler, Calder Miller, David Wellnitz, Sean R. Muleady, Junyu Lin, Krzysztof P. Zmarzki, Reuben R. W. Wang, John L. Bohn, Ana Maria Rey, and Jun Ye, “Observation of generalized t - J spin dynamics with tunable dipolar interactions,” *Science* **388**, 381–386 (2025), arXiv:2404.18916 [cond-mat.quant-gas].
- [37] Peter T. Brown, Elmer Guardado-Sanchez, Benjamin M. Spar, Edwin W. Huang, Thomas P. Devereaux, and Waseem S. Bakr, “Angle-resolved photoemission spectroscopy of a Fermi-Hubbard system,” *Nature Physics* **16**, 26–31 (2020), arXiv:1903.05678 [cond-mat.quant-gas].
- [38] Christian Gross and Waseem S. Bakr, “Quantum gas microscopy for single atom and spin detection,” *Nature Physics* **17**, 1316–1323 (2021), arXiv:2010.15407 [cond-mat.quant-gas].
- [39] Jayadev Vijayan, Pimonpan Sompert, Guillaume Salomon, Joannis Koeppell, Sarah Hirthe, Annabelle Bohrdt, Fabian Grusdt, Immanuel Bloch, and Christian Gross, “Time-resolved observation of spin-charge deconfinement in fermionic Hubbard chains,” *Science* **367**, 186–189 (2020), arXiv:1905.13638 [cond-mat.quant-gas].
- [40] Andrew J. Ferris and Guifre Vidal, “Perfect sampling with unitary tensor networks,” *Phys. Rev. B* **85**, 165146 (2012).
- [41] Jia-Long Wang, Shi-Jie Hu, and Xue-Feng Zhang, “Quantum colored strings in the hole-doped t - J_z model,” *Phys. Rev. B* **111**, 205121 (2025).
- [42] Annabelle Bohrdt, Lukas Homeier, Immanuel Bloch, Eugene Demler, and Fabian Grusdt, “Strong pairing in mixed-dimensional bilayer antiferromagnetic Mott insulators,” *Nature Physics* **18**, 651–656 (2022), arXiv:2108.04118 [cond-mat.str-el].
- [43] Sarah Hirthe, Thomas Chalopin, Dominik Bourgund, Petar Bojović, Annabelle Bohrdt, Eugene Demler, Fabian Grusdt, Immanuel Bloch, and Timon A. Hilker, “Magnetically mediated hole pairing in fermionic ladders of ultracold atoms,” *Nature (London)* **613**, 463–467 (2023), arXiv:2203.10027 [cond-mat.quant-gas].
- [44] Henning Schlömer, Hannah Lange, Titus Franz, Thomas Chalopin, Petar Bojović, Si Wang, Immanuel Bloch, Timon A. Hilker, Fabian Grusdt, and Annabelle Bohrdt, “Local control and mixed dimensions: Exploring high-temperature superconductivity in optical lattices,” *PRX Quantum* **5**, 040341 (2024).
- [45] P. Fulde and F. Pollmann, “Strings in strongly correlated electron systems,” *Annalen der Physik* **520**, 441–449 (2008), arXiv:0711.2129 [cond-mat.str-el].
- [46] Xue-Feng Zhang and Sebastian Eggert, “Chiral edge states and fractional charge separation in a system of interacting bosons on a kagome lattice,” *Phys. Rev. Lett.* **111**, 147201 (2013).
- [47] Zheng Zhou, Changle Liu, Zheng Yan, Yan Chen, and Xue-Feng Zhang, “Quantum dynamics of topological strings in a frustrated Ising antiferromagnet,” *npj Quantum Materials* **7**, 60 (2022), arXiv:2010.01750 [cond-mat.str-el].
- [48] Yuan Wan and Oleg Tchernyshyov, “Quantum strings in quantum spin ice,” *Phys. Rev. Lett.* **108**, 247210 (2012).
- [49] Xue-Feng Zhang, Shijie Hu, Axel Pelster, and Sebastian Eggert, “Quantum domain walls induce incommensurate supersolid phase on the anisotropic triangular lattice,” *Phys. Rev. Lett.* **117**, 193201 (2016).

END MATTER

DMRG.—For consistency in the following discussions, we always choose odd values for L_x . While selecting other values of L_x or using irregularly sheared open boundaries may introduce certain phases to spinon singlets, which does not alter conclusions regarding d -wave pairing. To prevent the formation of a frozen stripe, we double the value of J along the bonds connecting sites in the two edge columns [41]. In both the t - J and Hubbard models, we show benchmarks of three key quantities (i.e., truncation errors, the PPC function, the sampling data) below.

Effective Hamiltonian of a QCS.—When multiple holes are introduced into the AF background, they spontaneously organize into an individual stripe with a π -phase shift. This one-dimensional, curved structure is inherently quantum in nature due to electron hopping, distinguishing it from classical counterpart. As a result, it is referred to as a “quantum string” [45–49]. Building on our recent work [41], an individual stripe can be described by a QCS composed of three types of CPs. By imposing the constraint that only one CP is allowed per row, the restricted Hilbert space can be constructed, from which the effective Hamiltonian can be derived.

The t - J model can be extended to t - J - α model, which is explicitly written as

$$H = -t \sum_{\langle \ell, \ell' \rangle, \sigma} (f_{\ell, \sigma}^\dagger f_{\ell', \sigma} + \text{h.c.}) + J \sum_{\langle \ell, \ell' \rangle} \left[\alpha (S_\ell^x S_{\ell'}^x + S_\ell^y S_{\ell'}^y) + S_\ell^z S_{\ell'}^z - \frac{1}{4} n_\ell n_{\ell'} \right], \quad (\text{M1})$$

where the anisotropy parameter α is tunable. To derive the effective Hamiltonian of QCS, we introduce the effective spin field $\Gamma_{\bar{y}}^z \in \mathbb{Z}$, where \bar{y} labels the dual row in between rows y and $y+1$. The corresponding raising (lowering) operators of the effective spin field and CPs are denoted as $\Gamma_{\bar{y}}^+$ ($\Gamma_{\bar{y}}^-$) and c_χ^\dagger (c_χ), respectively. Without loss of generality, we choose the position of the CP in row $y=1$ to label the position of QCS, denoted as $\mathcal{X}^{(\text{CS})}$. Consequently, the electron configuration has a QCS representation: $|s\rangle = |\mathcal{X}^{(\text{CS})}, \{\Gamma^z\}, \{c_\chi\}\rangle$, where the sequences $\{\Gamma^z\}$ and $\{c_\chi\}$ represent the effective spin fields and CPs across all rows, respectively.

Building on the t - J - α model while neglecting local spin fluctuations inside the two AF domains, the effective model can be derived as:

$$H_e^{\text{CS}} = H_d + H_0^{(\text{g})} + H_0^{(\text{r-b/g-g})} + H_0^{(\text{r-g/g-r})} + H_0^{(\text{b-g/g-b})} + H_0^{(\text{ex1})} + H_0^{(\text{ex2})}. \quad (\text{M2})$$

The diagonal term H_d describes the diagonal tension energy. The off-diagonal terms describe various interaction processes between CPs: $H_0^{(\text{g})}$ accounts for electron hopping along the x -axis, while $H_0^{(\text{r-b/g-g})}$ captures the creation of an $\mathbf{r-b}$ pair and its reverse process, and the terms $H_0^{(\text{r-g/g-r})}$ ($H_0^{(\text{b-g/g-b})}$) describe the movement of spinons (dual-holes). In addition to these terms from the t - J_z model [41], the spin exchange interaction introduces two new terms, which are written as:

$$H_0^{(\text{ex1})} = J_\pm \sum_y n_y^{(\text{r})} \left[(\Gamma_{\bar{y}}^+)^4 (\Gamma_{\bar{y}-1}^-)^4 + \text{H.c.} \right], \quad (\text{M3})$$

and

$$H_0^{(\text{ex2})} = J_\pm \sum_y n_{y+1}^{(\text{r})} n_y^{(\text{r})} \left[(\Gamma_{\bar{y}+1}^+)^2 (\Gamma_{\bar{y}-1}^-)^2 + \text{H.c.} \right] \quad (\text{M4})$$

for $\Gamma_{\bar{y}}^z = 0$, where $J_\pm = \alpha J/2$. The spin exchange term $H_0^{(\text{ex1})}$ provides the kinetic energy of spinons in the x direction. The most critical term, $H_0^{(\text{ex2})}$, exchanges the chiralities of spinons

located in two adjacent rows, which is vital for identifying the spinon singlet, as demonstrated in Fig. 2(c).

As mentioned before, the spin exchange interaction within the AF ordered domains benefits the formation of spinon singlet, thereby lowering the ground-state energy. However, these local quantum fluctuations introduce significant noise into the statistical data of spinons, which can over-curtain the characteristic signals of spinons in QCSs. To prepare the ground-state wavefunction without these noises for the perfect sampling procedure outlined in this work, we apply an external staggered magnetic field to the two edge columns, pinning the polarization of spins within the AF domains along the z -axis by inducing a spin-rotation symmetry breaking (see details in **SM**). In QCSM, as described above, we focus solely on the spin exchange interaction relevant to spinons in QCSs and adjust the strength of this interaction to include additional renormalization effects from the AF domains. Following the above-mentioned instructions, with the spin exchange interaction strength doubled, we successfully reproduce a d -wave pattern for a 1/2 hole-doped stripe, as shown in Fig. 3(c), which closely resembles the DMRG-calculated pattern in Fig. 1(b). Meanwhile, the spinon correlation functions obtained from QCSM in Fig. 3(d) and DMRG in Fig. 2(b) exhibit a similar distribution.

SUPPLEMENTAL MATERIAL

A. PPC function

The d -wave pairing pattern means that the PPCs between x -bonds and y -bonds are negative, while those between x -bonds are positive. To complementing the data shown in the main text, we present the PPC functions of the Hubbard and t - J models starting from a target x -bond. As shown in Fig. S1 and Fig. S2, the PPC functions obtained from both DMRG and QCSM exhibit similar d -wave patterns.

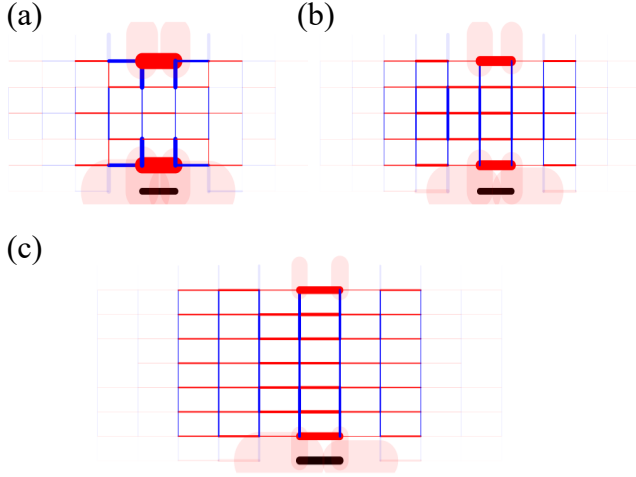


FIG. S1. The PPC function, starting from a target x -bond (black line), is calculated using DMRG in the Hubbard and t - J models. The parameters in (a-c) are the same as those used in Fig. 1(a), Fig. 3(b) and Fig. 1(b), respectively.

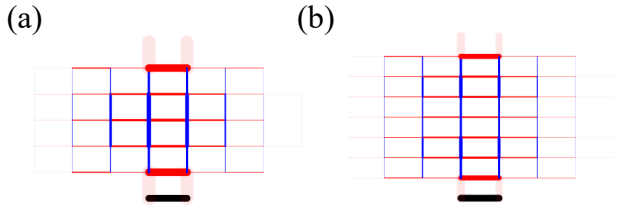


FIG. S2. The PPC function, starting from a target x -bond (black line), is calculated using QCSM in the t - J model. The parameters in (a,b) are the same as those used in Fig. 3(b) and Fig. 1(b), respectively.

B. Microscopic Mechanism of d -wave

In this section, we will discuss the underlying relation between spinon singlets and d -wave pairing pattern.

y - y bonds.—As explained in the main text, the PPC functions between two y -bonds are mainly contributed by the two-spinon bases $|s\rangle$ (left panel) and $|s'\rangle$ (right panel) demonstrated in Fig. S3. The chirality order of the spinon pair will change

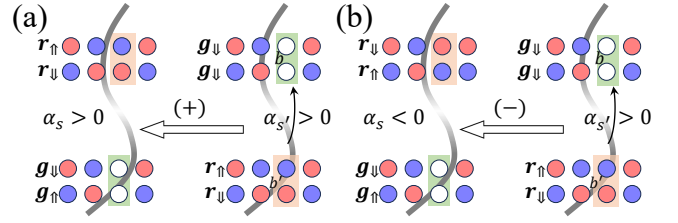


FIG. S3. Schematic diagrams illustrate the processes of moving a pair of electrons from y -bond b' to y -bond b (a) with and (b) without changing the chirality sequence.

if two electrons move to the positions of two holes, with a corresponding spin exchange. Therefore, the overall sign of the PPC function will always be positive.

x - y bonds.—The analysis in the main text lacks a discussion of Sgn_0 . As shown in Figs. S4(a,b), the sign of $(\mathbf{r}-\mathbf{b})/\mathbf{g}-\mathbf{g}$ process is closely related to the sign of the effective spin field between the holons [41]. However, by comparing Fig. S4(c) with Fig. 4(c), we find that although Sgn_0 introduces an additional negative sign in α_s , Sgn_Δ is also reversed simultaneously. Furthermore, the process shown in Fig. S4(d) can also contribute to the PPC function, but the sign of $\alpha_{s'}$ is dependent on the strength of the spin exchange interaction. Fortunately, the amplitude of $\alpha_{s'}$ is very small because two closely spaced spinons with large Γ_{ij}^z experience higher tension energy.

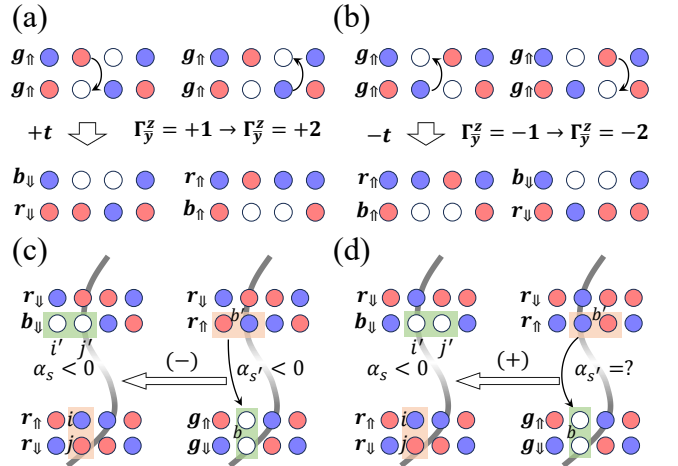


FIG. S4. Schematic diagrams for (a,b) $(\mathbf{r}-\mathbf{b})/\mathbf{g}-\mathbf{g}$ processes which gives different signs, and (c,d) illustrate the processes of moving an electron pair from x -bond b' to y -bond b . The negative sign of α_s result from the local fluctuation $\mathbf{r}-\mathbf{b}$ pair with positive effective spin field $\Gamma_{ij}^z = +2$.

x - x bonds.—The corresponding mechanism can also be understood using the QCSM framework established in the main text. Unlike other cases, the main contributions to the PCC between two x -bonds stem from the movement of an electron pair along the x -axis, involving two three-spinon bases, $|s\rangle$ and $|s'\rangle$, as depicted in Fig. S5. When a spin exchange operation occurs between Δ_b and $\Delta_{b'}$, the chirality sequence is

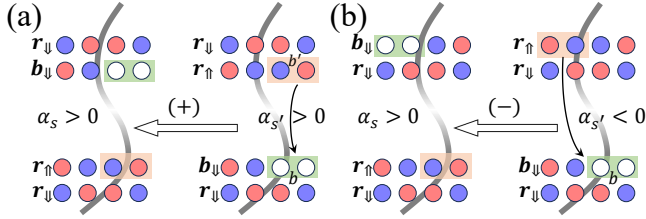


FIG. S5. Schematic diagrams illustrate the processes of moving an electron pair from x -bond b' to x -bond b (a) with and (b) without changing the chirality sequence.

altered. As a result, the sign of $G_{b,b'}^{s,s'}$ remains positive as long as the spinon-singlet is far from the \mathbf{r} - \mathbf{b} pair. Furthermore, other processes related to the PPC between x -bonds can also be analyzed similarly, with the overall conclusion remaining the same.

At last, the amplitude of a two-spinon basis is much larger than that of a three-spinon basis when J is not too small. So the strengths of the PPC function follow the general relation: x - x bonds $<$ x - y bonds $<$ y - y bonds. This implies that the d -wave is not isotropic in space, which may be attributed to the thin cylinders studied in the main text. However, since the local vacuum fluctuations, responsible for producing the \mathbf{r} - \mathbf{b} pairs, originates from electron hopping processes, the difference in the PPC function between the x and y directions is expected to become smaller when t/J increases.

C. Pinning field in the DMRG calculations

In the t - J model, to facilitate perfect sampling, we pin the AF order in the left and right domains along the specific z -axis, ensuring that the local spin fluctuations within AF domains do not contribute to the statistical data for spinons in QCSs. This operation breaks the spin rotational symmetry in both domains, which is protected by finite energy gaps between quasi-degenerate energy levels. Specifically, the pinning field adopts a staggered form, as shown in the inset of Fig. S6, applying a magnetic field along the z -axis with a magnitude of $\pm V_0$ to the red and blue sites, respectively.

In Fig. S6, we note that when the cylinder circumference is $L_y = 6$, the local magnetizations increase rapidly for a small pinning field magnitude V_0 , and this behavior becomes much more pronounced as the cylinder circumference increases, for example, when $L_y = 8$. This phenomenon indicates spontaneous magnetization, which would arise in the thermodynamical limit as both L_x and L_y approach infinity. As V_0 becomes large, the magnetization approaches a linear function of V_0 (red line), with a constant slope corresponding to the antiferromagnetic susceptibility. The line has a finite intercept with the y -axis, revealing a finite antiferromagnetic moment due to spontaneous magnetization at $V_0 = 0$. Notably, the system enters the symmetry-breaking region when $V_0 \gtrsim 0.1$.

We further show the benchmark for sampling data using two typical pinning field magnitudes in the symmetry-

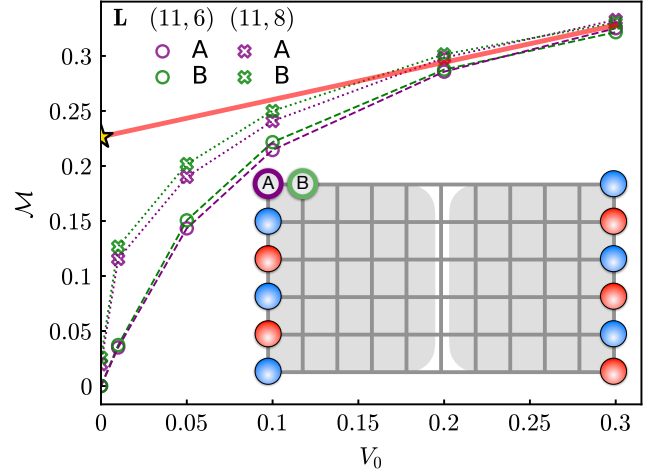


FIG. S6. Local magnetizations $\mathcal{M} = \langle S_\ell^z \rangle = \langle n_{\ell,\uparrow} - n_{\ell,\downarrow} \rangle$, for two specific lattice sites A (violet) and B (green), as a function of the pinning field magnitude V_0 . Specifically, a magnetic field along the positive and negative directions of the z -axis is applied to the blue and red sites, respectively, at two edge columns of the t - J model. For a finely-tuned V_0 , the orders in the left and right AF domains (grey shaded regions) are pinned along the z -axis. The other parameters are the same as those used in Fig. 1(b) and Fig. 3(d), respectively.

breaking region $V_0 = 0.1$ and 0.3 . In Fig. S7, we observe that the spinon correlation function for representative spinon distances consistently increases as V_0 increases, without changing the ordering of the spinon correlation values. Meanwhile, the snapshots for the spinon singlet with $(\delta x, \delta y) = (0, 1)$ dominate. Therefore, in the main text, we always use $V_0 = 0.3$ as the representative magnitude of the pinning field during the perfect sampling procedure. The ratios of count and weight for the snapshots with spinon singlets depending on the pin-

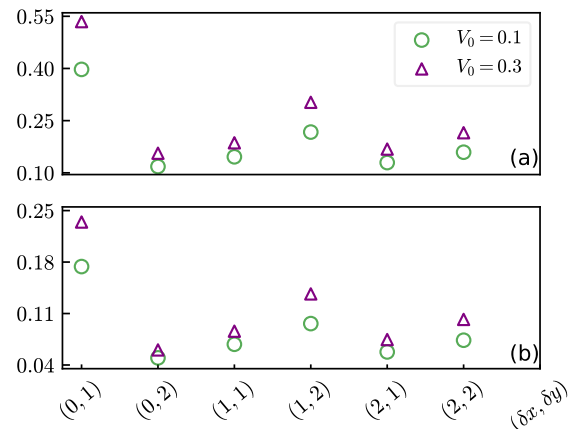


FIG. S7. Spinon correlation function with representative spinon distances $(\delta x, \delta y)$ for the t - J model. Here we make a comparison between $V_0 = 0.1$ and 0.3 when fixing the truncated bond dimension of $M = 8, 192$. The other parameters in the plots (a,b) are the same as those used in Fig. 1(b) and Fig. 3(d), respectively.

<i>t</i> - <i>J</i> model at <i>J</i> = 0.6				
A 1/2 hole-filled stripe with L = (11, 8)				
	count (%)		weight (%)	
<i>V</i> ₀	0.1	0.3	0.1	0.3
ratio	26.2	42.4	93.0	96.2
A 2/3 hole-filled stripe with L = (11, 6)				
	count (%)		weight (%)	
<i>V</i> ₀	0.1	0.3	0.1	0.3
ratio	15.7	21.2	56.0	55.6

TABLE I. The ratios of count and weight for the snapshots with spinon singlet pairs as a function of the pinning field magnitude V_0 , when $M = 8, 192$ is used in DMRG.

ning field magnitude are listed in Table I.

D. Systematic errors in the DMRG calculations

In Table II, we show the truncation errors for three distinct sets of hole filling in the stripe, cylinder circumference L_y , and other parameters in the Hubbard and *t*-*J* models studied in this work. We find that a truncated bond dimension of $M = 16,384$ ensures that the truncation errors are below or on the order of $\lesssim 10^{-4}$, when the pinning field is absent. With a finite pinning field, the truncation errors become consistently smaller compared to those for $V_0 = 0$.

Hubbard model at $t_2 = -0.2$ and $U = 12$					
A 2/3 hole-filled stripe with L = (9, 6)					
<i>M</i>	2,048	4,096	8,192	12,288	16,384
ϵ	/	/	1.19×10^{-4}	9.99×10^{-5}	9.00×10^{-5}
<i>t</i> - <i>J</i> model at $J = 0.6$					
A 2/3 hole-filled stripe with L = (11, 6)					
<i>M</i>	2,048	4,096	8,192	12,288	16,384
ϵ	2.31×10^{-4}	9.12×10^{-5}	3.15×10^{-5}	1.50×10^{-5}	8.47×10^{-6}
A 1/2 hole-filled stripe with L = (11, 8)					
<i>M</i>	2,048	4,096	8,192	12,288	16,384
ϵ	4.12×10^{-4}	2.95×10^{-4}	1.96×10^{-4}	1.28×10^{-4}	9.19×10^{-5}

TABLE II. The truncation errors ϵ as a function of the truncated bond dimension M used in DMRG, when the pinning field is absent.

We further benchmark the PPC function, starting from a target *y*-bond, along two given paths shown in the insets of Fig. S8. By varying the truncated bond dimensions from $M = 8, 192$ to 16,384 across three typical parameter sets, we find that the absolute values of the PPC function remain almost unchanged across a broad range, spanning two orders of magnitudes, e.g., from 10^{-2} to 10^{-5} as shown in Fig. S8(a). Therefore, the PCC function data presented in the main text is quantitatively reliable for demonstrating electron pairing.

In Fig. S9, we also present a benchmark of the statistical data obtained from the perfect sampling technique. As the truncated bond dimension M increases, we find that the spinon correlation function for representative spinon distances exhibit small errors well below the symbol sizes, for two specific parameter sets in the *t*-*J* model, as show in Figs. S9(b,c). In

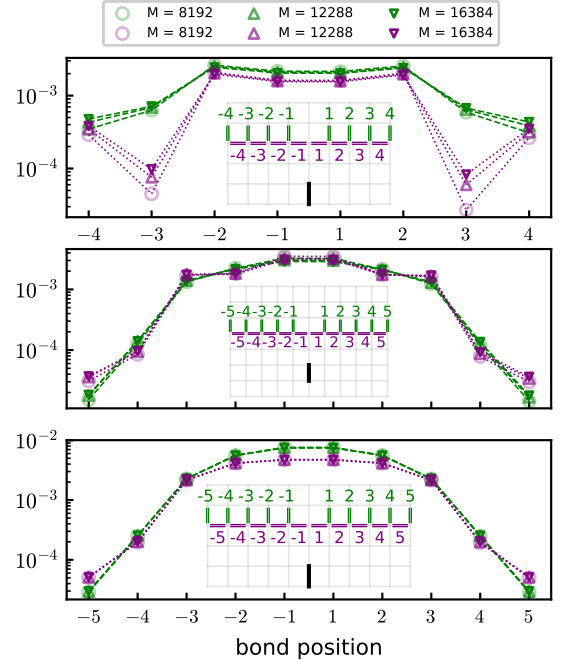


FIG. S8. The PPC function for *y*-*y* bonds (green symbols) and *y*-*x* bonds (violet symbols) as a function of the bond position for (a) the Hubbard model, and (b,c) the *t*-*J* model. Insets: the PPC function, starting from a target *y*-bond (black line), is measured along a path of *y*-bonds (green lines) and another path of *x*-bonds (violet lines) for a comparison. Numbers mark the bond positions. The other parameters are the same as those used in Figs. 1(a,b) and Fig. 3(d), respectively.

contrast, the Hubbard model shows a more noticeable change as M increases in Fig. S9(a). For the case of spinon distance (1, 2), the relative change is roughly less than 15% when comparing the data for $M = 8, 192$ and 16,384. Nevertheless, the snapshots for the spinon singlet with spinon distance (0, 1)

Hubbard model at $t_2 = -0.2$ and $U = 12$						
A 2/3 hole-filled stripe with L = (9, 6)						
	count (%)			weight (%)		
<i>M</i>	8,192	12,288	16,384	8,192	12,288	16,384
ratio	13.8	13.3	12.8	38.5	38.1	41.8
<i>t</i> - <i>J</i> model at $J = 0.6$						
A 1/2 hole-filled stripe with L = (11, 8)						
	count (%)			weight (%)		
<i>M</i>	8,192	12,288	16,384	8,192	12,288	16,384
ratio	42.4	42.0	42.0	96.2	96.1	96.0
A 2/3 hole-filled stripe with L = (11, 6)						
	count (%)			weight (%)		
<i>M</i>	8,192	12,288	16,384	8,192	12,288	16,384
ratio	21.2	21.3	21.2	55.6	55.7	56.1

TABLE III. The ratios of count and weight for the snapshots with spinon singlet pairs as a function of the truncated bond dimension M used in DMRG, when $V_0 = 0.3$.

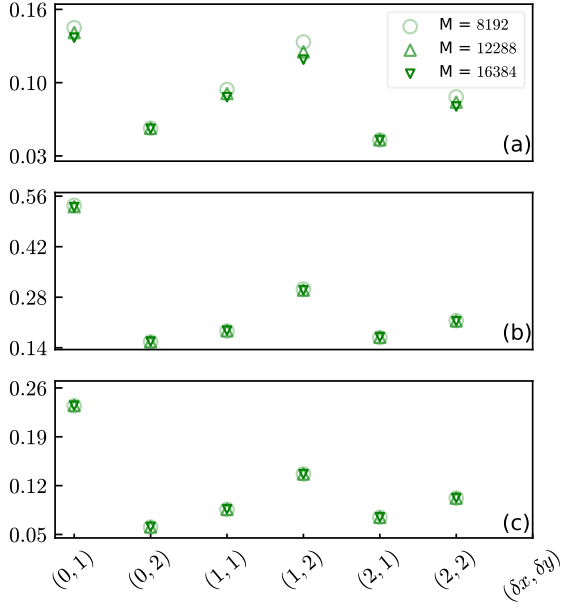


FIG. S9. Spinon correlation function with spinon distances $(\delta x, \delta y)$ for (a) the Hubbard model, and (b,c) the t - J model. The pinning field magnitude $V_0 = 0.3$ is used in the perfect sampling procedure. The other parameters are the same as those used in Figs. 1(a,b) and Fig. 3(d), respectively.

continue to dominate the ground-state wave functions, which is a key feature for determining the d -wave pairing pattern for electrons, as discussed in the main text. The ratios of count and weight for the snapshots with spinon singlets versus the truncated bond dimensions are listed in Table III.

E. Details of “unpaired” and “invalid”

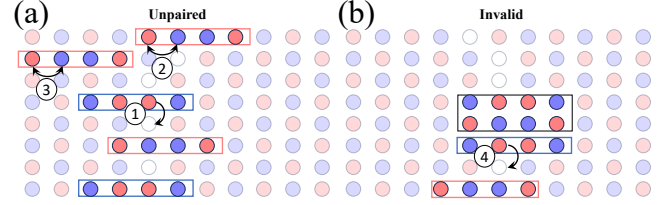


FIG. S10. The typical snapshots of (a) “unpaired” and (b) “invalid” cases for a 1/2 hole-doped stripe in the t - J model. The black arrows with numbers in circles label different dynamic processes. All the data are obtained via the perfect sampling technique, and the parameters are the same as those used in Fig. 1.

The appearance of “unpaired” and “invalid” samples can be understood by analyzing the typical snapshots presented in Figs. S10(a,b), respectively. Through the hopping process ① and spin-exchange process ②, the spinon pair can be restored. It is clear that these two consecutive processes enable the spinon pair to move in the y and x directions, respectively. Meanwhile, the quantum fluctuation process ③ can locally destroy the AF order, but such excitation is unstable due to its high energy cost. Therefore, “unpaired” samples mainly arise from local perturbations of “spinon singlet” states, which explains why many “unpaired” samples have apparently much smaller weights. The process ④ in Fig. 2(b) demonstrates that one spinon in a spinon singlet can meet another spinon singlet. However, it cannot break up two existing spinon singlets to form a new spinon singlet, which is the main reason for the “invalid” part.